K^{*0} production in Au + Au collisions at $\sqrt{s_{NN}}$ = 7.7, 11.5, 14.5, 19.6, 27, and 39 GeV from the RHIC beam energy scan

M. S. Abdallah,[1] B. E. Aboona,[2] J. Adam,[3] L. Adamczyk,[4] J. R. Adams,[5] J. K. Adkins,[6] I. Aggarwal,[7] M. M. Aggarwal,[7] Z. Ahammed,[8] D. M. Anderson,[2] E. C. Aschenauer,[9] J. Atchison,[10] V. Bairathi,[11] W. Baker,[12] J. G. Ball Cap,[13] K. Barish,[12] R. Bellwied,[13] P. Bhagat,[14] A. Bhasin,[14] S. Bhatta,[15] J. Bielcik,[3] J. Bielcikova,[16] J. D. Brandenburg,[9] X. Z. Cai,[17] H. Caines,[18] M. Calderón de la Barca Sánchez,[19] D. Cebra,[19] I. Chakaberia,[20] P. Chaloupka,[3] B. K. Chan,[21] Z. Chang,[22] A. Chatterjee,[23] D. Chen,[12] J. Chen,[24] J. H. Chen,[25] X. Chen,[26] Z. Chen,[24] J. Cheng,[27] Y. Cheng,[21] S. Choudhury,[25] W. Christie,[9] X. Chu,[9] H. J. Crawford,[28] M. Csanád,[29] G. Dale-Gau,[30] M. Daugherity,[10] I. M. Deppner,[31] A. Dhamija,[7] L. Di Carlo,[32] L. Didenko,[9] P. Dixit,[33] X. Dong,[20] J. L. Drachenberg,[10] E. Duckworth,[34] J. C. Dunlop,[9] J. Engelage,[28] G. Eppley,[35] S. Esumi,[36] O. Evdokimov,[30] A. Ewigleben,[37] O. Eyser,[9] R. Fatemi,[6] F. M. Fawzi,[1] S. Fazio,[38] C. J. Feng,[39] Y. Feng,[40] E. Finch,[41] Y. Fisyak,[9] C. Fu,[42] C. A. Gagliardi,[2] T. Galatyuk,[43] F. Geurts,[35] N. Ghimire,[44] A. Gibson,[45] K. Gopal,[46] X. Gou,[24] D. Grosnick,[45] A. Gupta,[14] W. Guryn,[9] A. Hamed,[1] Y. Han,[35] S. Harabasz,[43] M. D. Harasty,[19] J. W. Harris,[18] H. Harrison,[6] S. He,[42] W. He,[25] X. H. He,[47] Y. He,[24] S. Heppelmann,[19] N. Herrmann,[31] E. Hoffman,[13] L. Holub,[3] C. Hu,[47] Q. Hu,[47] Y. Hu,[20] H. Huang,[39] H. Z. Huang,[21] S. L. Huang,[15] T. Huang,[30] X. Huang,[27] Y. Huang,[27] T. J. Humanic,[5] D. Isenhower,[10] M. Isshiki,[36] W. W. Jacobs,[22] C. Jena,[46] A. Jentsch,[9] Y. Ji,[20] J. Jia,[9,15] K. Jiang,[26] C. Jin,[35] X. Ju,[26] E. G. Judd,[28] S. Kabana,[11] M. L. Kabir,[12] S. Kagamaster,[37] D. Kalinkin,[22,9] K. Kang,[27] D. Kapukchyan,[12] K. Kauder,[9] H. W. Ke,[9] D. Keane,[34] M. Kelsey,[32] Y. V. Khyzhniak,[5] D. P. Kikoła,[23] B. Kimelman,[19] D. Kincses,[29] I. Kisel,[48] A. Kiselev,[9] A. G. Knospe,[37] H. S. Ko,[20] L. K. Kosarzewski,[3] L. Kramarik,[3] L. Kumar,[7] S. Kumar,[47] R. Kunnawalkam Elayavalli,[18] J. H. Kwasizur,[22] R. Lacey,[15] S. Lan,[42] J. M. Landgraf,[9] J. Lauret,[9] A. Lebedev,[9] J. H. Lee,[9] Y. H. Leung,[31] N. Lewis,[9] C. Li,[24] C. Li,[26] W. Li,[17] W. Li,[35] X. Li,[26] Y. Li,[26] Y. Li,[27] Z. Li,[26] X. Liang,[12] Y. Liang,[34] R. Licenik,[16,3] T. Lin,[24] Y. Lin,[42] M. A. Lisa,[5] F. Liu,[42] H. Liu,[22] H. Liu,[42] T. Liu,[18] X. Liu,[5] Y. Liu,[2] T. Ljubicic,[9] W. J. Llope,[32] R. S. Longacre,[9] E. Loyd,[12] T. Lu,[47] N. S. Lukow,[44] X. F. Luo,[42] L. Ma,[25] R. Ma,[9] Y. G. Ma,[25] N. Magdy,[15] D. Mallick,[49] S. Margetis,[34] C. Markert,[50] H. S. Matis,[20] J. A. Mazer,[51] G. McNamara,[32] S. Mioduszewski,[2] B. Mohanty,[49] M. M. Mondal,[49] I. Mooney,[18] A. Mukherjee,[29] M. I. Nagy,[29] A. S. Nain,[7] J. D. Nam,[44] Md. Nasim,[33] K. Nayak,[46] D. Neff,[21] J. M. Nelson,[28] D. B. Nemes,[18] M. Nie,[24] T. Niida,[36] R. Nishitani,[36] T. Nonaka,[36] A. S. Nunes,[9] G. Odyniec,[20] A. Ogawa,[9] S. Oh,[20] K. Okubo,[36] B. S. Page,[9] R. Pak,[9] J. Pan,[2] A. Pandav,[49] A. K. Pandey,[36] T. Pani,[51] A. Paul,[12] B. Pawlik,[52] D. Pawlowska,[23] C. Perkins,[28] J. Pluta,[23] B. R. Pokhrel,[44] J. Porter,[20] M. Posik,[44] T. Protzman,[37] V. Prozorova,[3] N. K. Pruthi,[7] M. Przybycien,[4] J. Putschke,[32] Z. Qin,[27] H. Qiu,[47] A. Quintero,[44] C. Racz,[12] S. K. Radhakrishnan,[34] N. Raha,[32] R. L. Ray,[50] R. Reed,[37] H. G. Ritter,[20] M. Robotkova,[16,3] J. L. Romero,[19] D. Roy,[51] P. Roy Chowdhury,[23] L. Ruan,[9] A. K. Sahoo,[33] N. R. Sahoo,[24] H. Sako,[36] S. Salur,[51] S. Sato,[36] W. B. Schmidke,[9] N. Schmitz,[53] F-J. Seck,[43] J. Seger,[54] R. Seto,[12] P. Seyboth,[53] N. Shah,[55] P. V. Shanmuganathan,[9] M. Shao,[26] T. Shao,[25] R. Sharma,[46] A. I. Sheikh,[34] D. Y. Shen,[25] K. Shen,[26] S. S. Shi,[42] Y. Shi,[24] Q. Y. Shou,[25] E. P. Sichtermann,[20] R. Sikora,[4] J. Singh,[7] S. Singha,[47] P. Sinha,[46] M. J. Skoby,[56,40] N. Smirnov,[18] Y. Söhngen,[31] W. Solyst,[22] Y. Song,[18] B. Srivastava,[40] T. D. S. Stanislaus,[45] M. Stefaniak,[23] D. J. Stewart,[32] B. Stringfellow,[40] A. A. P. Suaide,[57] M. Sumbera,[16] C. Sun,[15] X. M. Sun,[42] X. Sun,[47] Y. Sun,[26] Y. Sun,[58] B. Surrow,[44] Z. W. Sweger,[19] P. Szymanski,[23] A. H. Tang,[9] Z. Tang,[26] T. Tarnowsky,[59] J. H. Thomas,[20] A. R. Timmins,[13] D. Tlusty,[54] T. Todoroki,[36] C. A. Tomkiel,[37] S. Trentalange,[21] R. E. Tribble,[2] P. Tribedy,[9] S. K. Tripathy,[29] T. Truhlar,[3] B. A. Trzeciak,[3] O. D. Tsai,[21,9] C. Y. Tsang,[34,9] Z. Tu,[9] T. Ullrich,[9] D. G. Underwood,[60,45] I. Upsal,[35] G. Van Buren,[9] J. Vanek,[9] I. Vassiliev,[48] V. Verkest,[32] F. Videbæk,[9] S. A. Voloshin,[32] F. Wang,[40] G. Wang,[21] J. S. Wang,[58] P. Wang,[26] X. Wang,[24] Y. Wang,[42] Y. Wang,[27] Z. Wang,[24] J. C. Webb,[9] P. C. Weidenkaff,[31] G. D. Westfall,[59] D. Wielanek,[23] H. Wieman,[20] G. Wilks,[30] S. W. Wissink,[22] R. Witt,[61] J. Wu,[42] J. Wu,[47] X. Wu,[21] Y. Wu,[12] B. Xi,[17] Z. G. Xiao,[27] G. Xie,[20] W. Xie,[40] H. Xu,[58] N. Xu,[20] Q. H. Xu,[24] Y. Xu,[24] Z. Xu,[9] Z. Xu,[21] G. Yan,[24] Z. Yan,[15] C. Yang,[24] Q. Yang,[24] S. Yang,[62] Y. Yang,[39] Z. Ye,[35] Z. Ye,[30] L. Yi,[24] K. Yip,[9] Y. Yu,[24] H. Zbroszczyk,[23] W. Zha,[26] C. Zhang,[15] D. Zhang,[42] J. Zhang,[24] S. Zhang,[26] S. Zhang,[25] Y. Zhang,[47] Y. Zhang,[26] Y. Zhang,[42] Z. J. Zhang,[39] Z. Zhang,[9] Z. Zhang,[30] F. Zhao,[47] J. Zhao,[25] M. Zhao,[9] C. Zhou,[25] J. Zhou,[26] Y. Zhou,[42] X. Zhu,[27] M. Zurek,[60] and M. Zyzak[48]

(STAR Collaboration)

[1]*American University of Cairo, New Cairo 11835, New Cairo, Egypt*
[2]*Texas A&M University, College Station, Texas 77843*
[3]*Czech Technical University in Prague, FNSPE, Prague 115 19, Czech Republic*
[4]*AGH University of Science and Technology, FPACS, Cracow 30-059, Poland*
[5]*Ohio State University, Columbus, Ohio 43210*
[6]*University of Kentucky, Lexington, Kentucky 40506-0055*
[7]*Panjab University, Chandigarh 160014, India*
[8]*Variable Energy Cyclotron Centre, Kolkata 700064, India*
[9]*Brookhaven National Laboratory, Upton, New York 11973*
[10]*Abilene Christian University, Abilene, Texas 79699*

[11]*Instituto de Alta Investigación, Universidad de Tarapacá, Arica 1000000, Chile*
[12]*University of California, Riverside, California 92521*
[13]*University of Houston, Houston, Texas 77204*
[14]*University of Jammu, Jammu 180001, India*
[15]*State University of New York, Stony Brook, New York 11794*
[16]*Nuclear Physics Institute of the CAS, Rez 250 68, Czech Republic*
[17]*Shanghai Institute of Applied Physics, Chinese Academy of Sciences, Shanghai 201800*
[18]*Yale University, New Haven, Connecticut 06520*
[19]*University of California, Davis, California 95616*
[20]*Lawrence Berkeley National Laboratory, Berkeley, California 94720*
[21]*University of California, Los Angeles, California 90095*
[22]*Indiana University, Bloomington, Indiana 47408*
[23]*Warsaw University of Technology, Warsaw 00-661, Poland*
[24]*Shandong University, Qingdao, Shandong 266237*
[25]*Fudan University, Shanghai, 200433*
[26]*University of Science and Technology of China, Hefei, Anhui 230026*
[27]*Tsinghua University, Beijing 100084*
[28]*University of California, Berkeley, California 94720*
[29]*ELTE Eötvös Loránd University, Budapest, Hungary H-1117*
[30]*University of Illinois at Chicago, Chicago, Illinois 60607*
[31]*University of Heidelberg, Heidelberg 69120, Germany*
[32]*Wayne State University, Detroit, Michigan 48201*
[33]*Indian Institute of Science Education and Research (IISER), Berhampur 760010, India*
[34]*Kent State University, Kent, Ohio 44242*
[35]*Rice University, Houston, Texas 77251*
[36]*University of Tsukuba, Tsukuba, Ibaraki 305-8571, Japan*
[37]*Lehigh University, Bethlehem, Pennsylvania 18015*
[38]*University of Calabria & INFN-Cosenza, Italy*
[39]*National Cheng Kung University, Tainan 70101*
[40]*Purdue University, West Lafayette, Indiana 47907*
[41]*Southern Connecticut State University, New Haven, Connecticut 06515*
[42]*Central China Normal University, Wuhan, Hubei 430079*
[43]*Technische Universität Darmstadt, Darmstadt 64289, Germany*
[44]*Temple University, Philadelphia, Pennsylvania 19122*
[45]*Valparaiso University, Valparaiso, Indiana 46383*
[46]*Indian Institute of Science Education and Research (IISER) Tirupati, Tirupati 517507, India*
[47]*Institute of Modern Physics, Chinese Academy of Sciences, Lanzhou, Gansu 730000*
[48]*Frankfurt Institute for Advanced Studies FIAS, Frankfurt 60438, Germany*
[49]*National Institute of Science Education and Research, HBNI, Jatni 752050, India*
[50]*University of Texas, Austin, Texas 78712*
[51]*Rutgers University, Piscataway, New Jersey 08854*
[52]*Institute of Nuclear Physics PAN, Cracow 31-342, Poland*
[53]*Max-Planck-Institut für Physik, Munich 80805, Germany*
[54]*Creighton University, Omaha, Nebraska 68178*
[55]*Indian Institute Technology, Patna, Bihar 801106, India*
[56]*Ball State University, Muncie, Indiana 47306*
[57]*Universidade de São Paulo, São Paulo, Brazil 05314-970*
[58]*Huzhou University, Huzhou, Zhejiang 313000*
[59]*Michigan State University, East Lansing, Michigan 48824*
[60]*Argonne National Laboratory, Argonne, Illinois 60439*
[61]*United States Naval Academy, Annapolis, Maryland 21402*
[62]*South China Normal University, Guangzhou, Guangdong 510631*

(Received 7 October 2022; accepted 15 December 2022; published 14 March 2023)

We report the measurement of K^{*0} meson at midrapidity ($|y| < 1.0$) in Au + Au collisions at $\sqrt{s_{NN}} = 7.7$, 11.5, 14.5, 19.6, 27, and 39 GeV collected by the STAR experiment during the Relativistic Heavy Ion Collider (RHIC) beam energy scan program. The transverse momentum spectra, yield, and average transverse momentum of K^{*0} are presented as functions of collision centrality and beam energy. The K^{*0}/K yield ratios are presented for

different collision centrality intervals and beam energies. The K^{*0}/K ratio in heavy-ion collisions are observed to be smaller than that in small-system collisions ($e + e$ and $p + p$). The K^{*0}/K ratio follows a similar centrality dependence to that observed in previous RHIC and Large Hadron Collider measurements. The data favor the scenario of the dominance of hadronic rescattering over regeneration for K^{*0} production in the hadronic phase of the medium.

DOI: 10.1103/PhysRevC.107.034907

I. INTRODUCTION

Resonances are very short-lived particles and provide an excellent probe of properties of QCD medium in heavy-ion collisions (HIC) [1]. They decay through strong interactions within roughly 10^{-23} seconds or a few fm/c which is of a similar order to the lifetime of the medium created in heavy-ion collisions. Due to their short lifetime, some resonances decay within the medium. Hence, they are subjected to in-medium interactions. During the evolution of HIC, the chemical (CFO) and kinetic (KFO) freeze-out temperatures play important roles. At CFO, the inelastic interactions among the constituents are expected to cease [2–7]. Afterward, the constituents can interact among themselves via elastic (or pseudoelastic) interactions until the KFO, when their mean free path increases and all interactions cease. Between CFO and KFO, there can be two competing effects, rescattering and regeneration. The momentum of resonance daughters (e.g., pions and kaons from K^{*0}) can be altered due to the scattering with other hadrons present in the medium. Thus the parent resonance (e.g., K^{*0}) is not reconstructible using the rescattered daughters. This may result in a reduced resonance yield. On the other hand, resonances may be regenerated via pseudoelastic interactions (e.g., $\pi K \leftrightarrow K^{*0}$) until KFO is reached. Such regeneration may result in an increase of resonance yield. The K^{*0} regeneration depends on the kaon-pion interaction cross section ($\sigma_{K\pi}$), the timescale allowed for this regeneration, and the medium density. The rescattering depends on resonance lifetime, daughter particle's interaction cross section with the medium (e.g., $\sigma_{K\pi,\,\pi\pi,\,KK}$), the medium density, and the timescale between CFO and KFO. The final resonance (e.g., K^{*0}) yield is affected by the relative strength of these two competing processes. Since the $\sigma_{\pi\pi}$ is about a factor of five larger than $\sigma_{K\pi}$ [8–10], one naively expects a loss of K^{*0} signal due to rescattering over regeneration. Furthermore, the mass peak position and width of resonances may be modified due to in-medium effects and late-stage rescattering.

Due to the short lifetime of about 4.16 fm/c, the K^{*0} meson is one of the ideal candidates to probe the hadronic phase of the medium between CFO and KFO. If rescattering plays a dominant role, then one naively expects a smaller resonance to nonresonance particle yield ratio (e.g., K^{*0}/K) in central collisions compared to that in peripheral and small-system ($p + p$) collisions. On the contrary, if regeneration is dominant, then the above ratio is expected to be larger in central compared to peripheral (and small-system) collisions. In previous Relativistic Heavy Ion Collider (RHIC) [11–15], SPS [16,17], and Large Hadron Collider (LHC) [18–24] measurements, it is observed that the K^{*0}/K ratio is indeed smaller in central heavy-ion collisions than in peripheral and elementary (e.g., $p + p$) collisions. The observation indicates the dominance of hadronic rescattering over regeneration. Such an observation is also supported by several transport model calculations [25–27]. The measurement of K^{*0} in the beam energy scan (BES) range can provide information on the interactions in the hadronic phase of the medium at these energies.

In this article, we report on the measurement of K^{*0} mesons at midrapidity ($|y| < 1.0$) using data from Au + Au collisions at $\sqrt{s_{NN}} = 7.7$, 11.5, 14.5, 19.6, 27, and 39 GeV collected by the STAR experiment during 2010-2014 in the first phase of the beam energy scan (called BES-I) program. The paper is organized as follows: Section II briefly describes the subdetectors of STAR used in this analysis along with the event and track selection criteria and the data-analysis methods. The results for K^{*0} mesons, which include transverse momentum (p_{T}) spectra, yield (dN/dy), average transverse momentum ($\langle p_{\mathrm{T}} \rangle$) and ratios to nonresonances are discussed in Sec. III. The results are summarized in Sec. IV.

II. EXPERIMENTAL DETAILS AND DATA ANALYSIS

A. STAR detector

The details of the STAR detector system are discussed in Reference [28]. The detector configuration during 2010 and 2011 are similar, while during 2014 the Heavy Flavor Tracker [29] was installed inside the Time Projection Chamber (TPC). Minimum-bias events are selected using the scintillator-based Beam Beam Counter (BBC) detectors. The BBCs are located on the two sides of the beam pipe in the pseudorapidity range $3.3 < |\eta| < 5.0$. The TPC [30] is the main tracking detector in STAR and is used for track reconstruction for the decay daughters of K^{*0}. The TPC has an acceptance of ± 1.0 in pseudorapidity and 2π in azimuth. With the TPC, one can identify particles in the low-momentum range by utilizing energy loss (dE/dx) and momentum information. The Time of Flight (TOF) [31,32] detector can be used to identify particles in the momentum region where the TPC dE/dx bands for pions and kaons overlap. The TOF works on the principle of Multigap Resistive Plate Chamber technology and provides pseudorapidity coverage $|\eta| < 0.9$ with full 2π azimuth.

B. Event selection

Minimum-bias events are selected using the coincidence between the BBC detectors [33]. The primary vertex of each event is reconstructed by finding the best common point from which most of the primary tracks originate. The vertex position along the beam direction (V_z) is required to be within ± 50 cm for $\sqrt{s_{NN}} \geqslant 11.5$ GeV and ± 70 cm for 7.7 GeV

TABLE I. Au+Au collision datasets, vertex position V_z and V_r selection, number of events analyzed.

Year	Energy (GeV)	$\lvert V_Z\rvert$ (cm)	V_r (cm)	Events (M)
2010	7.7	<70	<2	4.7
2010	11.5	<50	<2	12.1
2014	14.5	<50	<1	15.3
2011	19.6	<50	<2	27.7
2011	27	<50	<2	53.7
2010	39	<50	<2	128.5

in a coordinate system whose origin is at the center of TPC. The vertex in radial direction ($V_r = \sqrt{V_x^2 + V_y^2}$) is required to be smaller than 2.0 cm for all energies except 14.5 GeV where the vertex is not centered at (0, 0) in the xy plane and slightly offset at (0.0, −0.89). Hence the V_r is selected to be $V_r = \sqrt{V_x^2 + (V_y + 0.89)^2} < 1$ cm for 14.5 GeV [34]. The V_r selection excludes events where the incoming Au nuclei collide with the beam pipe. The above vertex selection criteria also ensure uniform acceptance within the η range ($|\eta| < 1.0$) studied. A typical vertex resolution 350 μm can be achieved using about 1000 tracks with a maximum 45 hit points in TPC [35]. The number of good events selected after these criteria are listed in Table I.

C. Centrality selection

The collision centrality is determined via a fit to the charged particle distribution within $|\eta| < 0.5$ in the TPC using a Glauber Monte Carlo simulation [36]. The minimum bias triggered events are divided into nine different intervals as 0–5%, 5–10%, 10–20%, 20–30%, 30–40%, 40–50%, 50–60%, 60–70%, and 70–80%. The average number of participant nucleons $\langle N_{\rm part}\rangle$ for BES-I energies are evaluated using a Glauber simulation and are reported in Refs. [34,37].

D. Track selection

Good quality tracks are selected by requiring at least 15 hit points in the TPC. In order to reduce track splitting, the tracks are required to include more than 55% of the maximum number of hits possible for their geometry. Particles are required to have transverse momentum greater than 0.15 GeV/c. To reduce contamination from secondary particles (e.g., weak decay contributions), the distance of closest approach (DCA) to the primary vertex is required to be smaller than 2 cm. Last, to ensure uniform acceptance, tracks are required to fall within ±1 in pseudorapidity.

E. Particle identification

Particle identification (PID) is carried out utilizing both the TPC and TOF detectors. The pion and kaon candidates are identified using the energy loss dE/dx of the particles inside the TPC. In the STAR TPC, pions and kaons can be distinguished up to about 0.7 GeV/c in momenta, while (anti-) protons can be distinguished up to about 1.1 GeV/c in momenta. Particle tracks in the TPC are characterized by the $N\sigma$ variable, which is defined as:

$$N\sigma(\pi, K) = \frac{1}{R}\log\frac{(dE/dx)_{\rm meas.}}{\langle dE/dx\rangle_{\rm theo.}}, \tag{1}$$

where the $(dE/dx)_{\rm meas.}$ is the measured energy loss inside the TPC for a track, $\langle dE/dx\rangle_{\rm theo.}$ is the expected mean energy loss from a parameterized Bichsel function [38], and R is the dE/dx resolution which is about 8.1%. The $N\sigma$ distribution is nearly Gaussian at a given momentum and calibrated to be centered at zero for each particle species with a width of unity [39].

The TOF detector extends the particle identification capabilities to intermediate and high p_T. The TOF system consists of TOF trays and Vertex Position Detectors. By measuring the time of flight of each particle, we can calculate mass-squared ($\rm m^2$) of the corresponding track,

$$m^2 = p^2[(t_{\rm TOF} \times c/l)^2 - 1], \tag{2}$$

where p is the momentum, $t_{\rm TOF}$ is the time of flight, c is the speed of light in vacuum, and l is the flight path length of the particle. The time resolution of TOF is about ≈80–100 ps. Using the information from the TOF, pions and kaons can be separated up to $p \approx 1.6$ GeV/c, and protons and kaons up to $p \approx 3.0$ GeV/c [39]. If the TOF-information is available, then $-0.2 < \rm m^2 < 0.15$ $[\rm GeV/c^2]^2$ and $0.16 < \rm m^2 < 0.36$ $[\rm GeV/c^2]^2$ is required for selecting pions and kaons, respectively. Otherwise we use the TPC $|N\sigma(\pi/K)| < 2.0$ to select pions or kaons.

F. K^{*0} reconstruction

The K^{*0} (and its antiparticle $\overline{K}^{*0}$) is reconstructed from its hadronic decay channel $K^{*0}(\overline{K}^{*0}) \to \pi^- K^+(\pi^+ K^-)$ (branching ratio 66%) [40]. The measurements are performed with the same collision centrality intervals (10%) for all energies except for $\sqrt{s_{NN}} = 7.7$ GeV, where the intervals are changed from 10% to 20% due to the low charged particle multiplicity at this energy. The analysis is done by combining both K^{*0} and $\overline{K}^{*0}$, which in the text is denoted by K^{*0}, unless specified.

In a typical event, it is impossible to distinguish the decay daughters of K^{*0} from other primary tracks. First, the invariant mass is reconstructed from the unlike sign $K\pi$ pairs in an event (called same-event pairs). The resultant invariant mass distribution contains true K^{*0} signal and a large random combinatorial background. Due to the large combinatorial background, the K^{*0} invariant mass peak is not visible. The typical signal-to-background ratio is within the range 0.002–0.02. Hence, the background must be subtracted from the same event distribution. The random combinatorial background is estimated using the daughter track rotation technique. In this analysis, the azimuthal angle of kaon track is rotated by 180° in a plane normal to particle's momentum vector, which breaks the correlation among the pairs originating from same parent particle. The K^{*0} invariant mass peak is obtained after subtracting the invariant mass distribution of the rotated tracks from the same event invariant mass distribution. The signal peak is observed on top of a residual background. The significance of K^{*0} signal is within the range 5–80 for all beam energies and centralities. It has been observed that

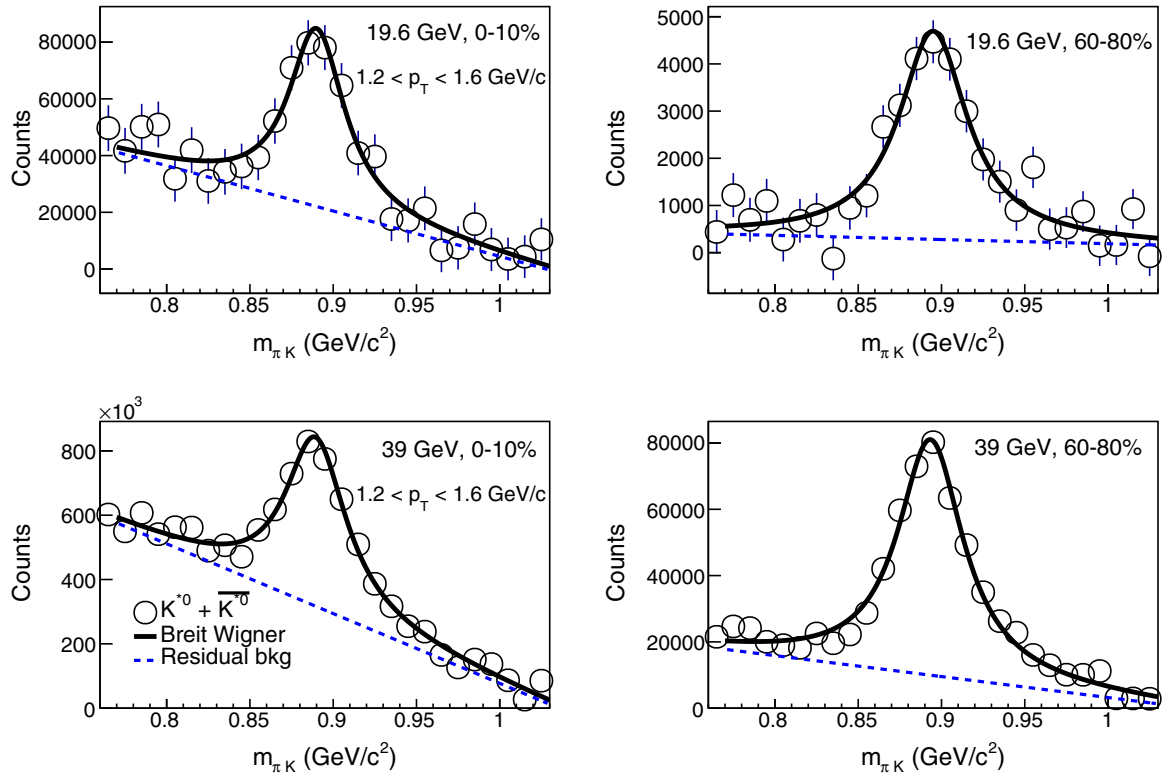

FIG. 1. The track-rotation combinatorial background subtracted $K\pi$ invariant mass distribution for the $1.2 < p_T < 1.6$ GeV/c (14.5 and 39 GeV). The data are fitted with a Breit-Wigner function plus a first-order polynomial [as given in Eq. (3)] by the solid line. The dashed line represents the residual background only. The uncertainties on the data points are statistical only and shown by bars.

the residual background may originate from correlated real $K\pi$ pairs from particle decays, correlated pairs from jets, or correlated misidentified pairs [12].

Figure 1 presents the K^{*0} invariant mass signal in the range $1.2 < p_T < 1.6$ GeV/c for two beam energies, $\sqrt{s_{NN}} = 14.5$ and 39 GeV, and for two centralities, 0–10% and 60–80%. The K^{*0} invariant mass distribution is obtained in different transverse momentum bins for different collision centrality intervals for six colliding beam energies. It is fitted with a Breit-Wigner and a first-order polynomial function and is defined by

$$\frac{dN}{dm_{\pi K}} = \frac{Y}{2\pi} \times \frac{\Gamma_0}{(m_{\pi K} - M_0)^2 + \frac{\Gamma_0^2}{4}} + (Am_{\pi K} + B), \quad (3)$$

The Breit-Wigner function describes the signal distribution while the first-order polynomial is included to account for the residual background. Here Y is the area under the Breit-Wigner function and M_0 and Γ_0 are the mass and width of K^{*0}. The K^{*0} invariant mass distribution is fitted within $0.77 < m_{\pi K} < 1.04$ GeV/c^2. The invariant mass peak and width of K^{*0} are found to be consistent within uncertainty with previously published STAR measurements in Au + Au and $p + p$ collisions (not shown here) at $\sqrt{s_{NN}} = 200$ GeV [11–14]. Since the mass and width are consistent between heavy-ion and $p + p$ collisions, it indicates that the K^{*0} line shape may not offer sensitivity to in-medium interactions and rescattering. Since the K^{*0} width is consistent with PDG value within uncertainty, the yield is calculated by keeping the width fixed to the vacuum value to avoid any statistical fluctuation. The boundary of the fitting range is varied within 0.01–0.02 GeV/c^2. The resulting variation in the K^{*0} yield is incorporated into the systematic uncertainties. The variation in residual background functions (first- and second-order polynomials) is also included in the systematic uncertainties. The yield of the K^{*0} is extracted in each p_T and collision centrality interval by integrating the background subtracted invariant mass distribution in the range of $0.77 < m_{\pi K} < 1.04$ GeV/c^2, subtracting the integral of the residual background function in the same range, and correcting the result to account for the yield outside this region by using the fitted Breit-Wigner function. This correction is about $\approx 10\%$ of the K^{*0} yield. Alternatively, the yield is extracted by integrating the fitted Breit-Wigner function only. The difference in the measured yield from various yield extraction method is about 5%. As a consistency check, the combinatorial background is also estimated from a mixed event technique. The resultant yield of K^{*0} after the background subtraction is found to be consistent with that from the track rotation method within uncertainties.

G. Detector acceptance and reconstruction and PID efficiency correction

The detector acceptance and the reconstruction efficiency ($\epsilon_{\text{acc}\times\text{rec}}$) is calculated by using the STAR embedding method. In this process, first K^{*0} is generated with uniform rapidity

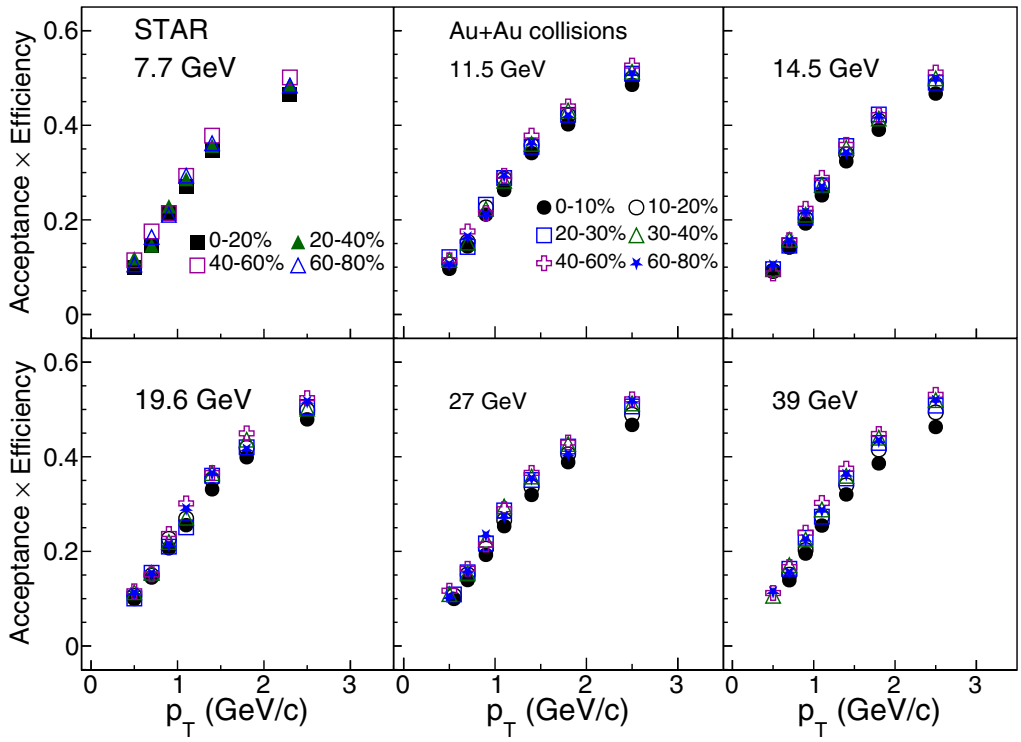

FIG. 2. The detector efficiency × acceptance in reconstructing the K^{*0} at various collision centralities in Au + Au collisions at $\sqrt{s_{NN}} =$ 7.7, 11.5, 14.5, 19.6, 27, and 39 GeV. The statistical uncertainties are within the marker size.

($|y| < 1.0$), $p_T (0 < p_T < 10$ GeV/c), and ϕ ($0 < \phi < 2\pi$) distribution. The number of K^{*0}s generated is about 5% of the total multiplicity of the event. Then the K^{*0} is decayed and its daughters are passed through the STAR detector simulation in GEANT3 and the TPC Response Simulator [41]. The simulated electronic signals are then combined with real data signals to produce a "combined event." This combined event is then passed through the standard STAR reconstruction chain. The reconstruction efficiency × acceptance ($\epsilon_{\text{acc}\times\text{rec}}$) is the ratio of the number of reconstructed K^{*0}s after passing through detector simulation with the same event/track selection parameters used in real data analysis to the input simulated number of K^{*0}s within the same rapidity ($|y| < 1.0$) interval. Figure 2 presents the detector acceptance and reconstruction efficiency as a function of p_T for different collision centrality intervals in $\sqrt{s_{NN}} = 7.7$, 11.5, 14.5, 19.6, 27, and 39 GeV collisions. The absence of clear centrality dependence in $\epsilon_{\text{acc}\times\text{rec}}$ could be due to the small variation in total multiplicity across the collision centrality and beam energy studied.

The particle identification efficiency (ϵ_{PID}) accounts for loss of particles due to TPC $N\sigma$ and TOF mass-squared cuts on K^{*0} daughters. The ϵ_{PID} is the product of efficiencies for each decay daughters. The PID efficiency is calculated using the $N\sigma$ and mass-squared distributions in real data. When the $N\sigma$ cuts are applied on pions and kaons, ϵ_{PID} for TPC is about 91.1% and for TOF it is more than 95%.

H. Systematic uncertainty

The systematic uncertainties are evaluated bin by bin for p_T spectra, yield, and $\langle p_T \rangle$ of K^{*0}. The sources of systematic uncertainties in the measurement are (i) signal extraction, (ii) yield extraction, (iii) event and track selections, (iv) particle identification, and (v) global tracking efficiency. The systematic uncertainties due to signal extraction are assessed by varying the invariant mass fit range, residual background function (first-order versus second-order polynomial) and the invariant mass fit function (nonrelativistic versus p-wave relativistic Breit-Wigner function [12]). The systematic in yield calculation is obtained by using histogram integration versus functional integration of the invariant mass distributions. Furthermore, the yield is calculated by keeping the width as a free parameter and fixed to the vacuum value. The variation in the yields are incorporated into the systematic uncertainties. The bounds of event, track quality, and particle identification selection cuts are varied by ≈10–20% (e.g., V_z selection variation; number of hits in TPC, |DCA|, $|N\sigma|$ and TOF-mass^2 variations), and the resulting difference is included into systematic uncertainties. The uncertainty due to global tracking efficiency is estimated to be 5% for charged particles [37], which results in 7.1% for track pairs for K^{*0}. The systematic uncertainty in dN/dy and $\langle p_T \rangle$ due to the low p_T extrapolations are obtained by using different fit functions (p_T and m_T exponential and Boltzmann [37]) compared to the default Tsallis fit function [42]. The systematic uncertainties for each of the above sources are calculated as (maximum − minimum)/$\sqrt{12}$ assuming uniform probability distributions between the maximum and minimum values. The final systematic uncertainty is the quadratic sum of the systematic uncertainties for each of the above sources [(i)–(v)]. The typical average systematic uncertainties in p_T

TABLE II. Systematic uncertainties for the p_T spectra, dN/dy, and $\langle p_T \rangle$ of K^{*0} at $\sqrt{s_{NN}} = 7.7$–39 GeV.

Systematic uncertainties	spectra	dN/dy	$\langle p_T \rangle$
Fitting region	1–3%	1%	1%
Residual background	2–4%	1–2%	1%
Fitting function	≈1%	≈1%	≈1%
Yield extraction	4%	4%	1%
Particle identification	2–5%	1–2%	1–2%
Track selection	1–3%	1–2%	1–2%
Tracking efficiency	7.1%	7.1%	7.1%
Low p_T extrapolation	–	5–6%	3%
Width fix/free	2–3%	2–3%	1%
Total	9–12%	10–11%	8–8.5%

spectra, dN/dy, and $\langle p_T \rangle$ from the above sources are listed in Table II.

III. RESULTS

A. Transverse momentum spectra

The raw yield of K^{*0} is normalized to the number of events ($N_{\rm evt}$), corrected for detector acceptance × reconstruction efficiency ($\epsilon_{\rm acc\times rec}$), particle identification efficiency ($\epsilon_{\rm PID}$), and branching ratio (BR),

$$\frac{d^2N}{dp_T dy} = \frac{1}{N_{\rm evt}} \times \frac{N^{\rm raw}}{dy dp_T} \times \frac{1}{\epsilon_{\rm acc\times rec} \times \epsilon_{\rm PID} \times {\rm BR}}, \quad (4)$$

Figure 3 presents the K^{*0} p_T spectra at midrapidity ($|y| < 1.0$) for various collision centrality intervals in Au + Au collisions at $\sqrt{s_{NN}} = 7.7$, 11.5, 14.5, 19.6, 27, and 39 GeV. The data are fitted with a Tsallis function [42] and defined by

$$\frac{d^2N}{dp_T dy} = p_T \frac{(n-1)(n-2)}{nT + [nT + m(n-2)]} \frac{dN}{dy} \left(1 + \frac{m_T - m}{nT}\right)^n, \quad (5)$$

where $m_T = \sqrt{m^2 + p_T^2}$, T is the inverse slope parameter, and n is the exponent. The Tsallis function describes both the exponential shape at low p_T and power law at high p_T. The Tsallis function is found to fit the spectra reasonably well across all the collision centrality intervals and beam energies with $\chi^2/{\rm NDF} < 2$. The Tsallis fit is used to extrapolate the yield in the unmeasured p_T regions. The typical range of fit parameters obtained are 12–100 for n and 150–285 MeV for T, respectively.

B. Yield and mean transverse momentum

The K^{*0} dN/dy is calculated using measured p_T spectra and assuming Tsallis fit function for extrapolation into the unmeasured p_T region. The low p_T extrapolation accounts for 20–40% of K^{*0} yield. Figure 4 presents the K^{*0} dN/dy as a function of average number of participating nucleons ($\langle N_{\rm part} \rangle$) in Au + Au collisions at $\sqrt{s_{NN}} = 7.7$, 11.5, 14.5, 19.6, 27, and 39 GeV. The dN/dy is approximately linear with $\langle N_{\rm part} \rangle$. Figure 5 presents the centrality dependence of dN/dy per average number of participant nucleons for K^{*0}. Results are

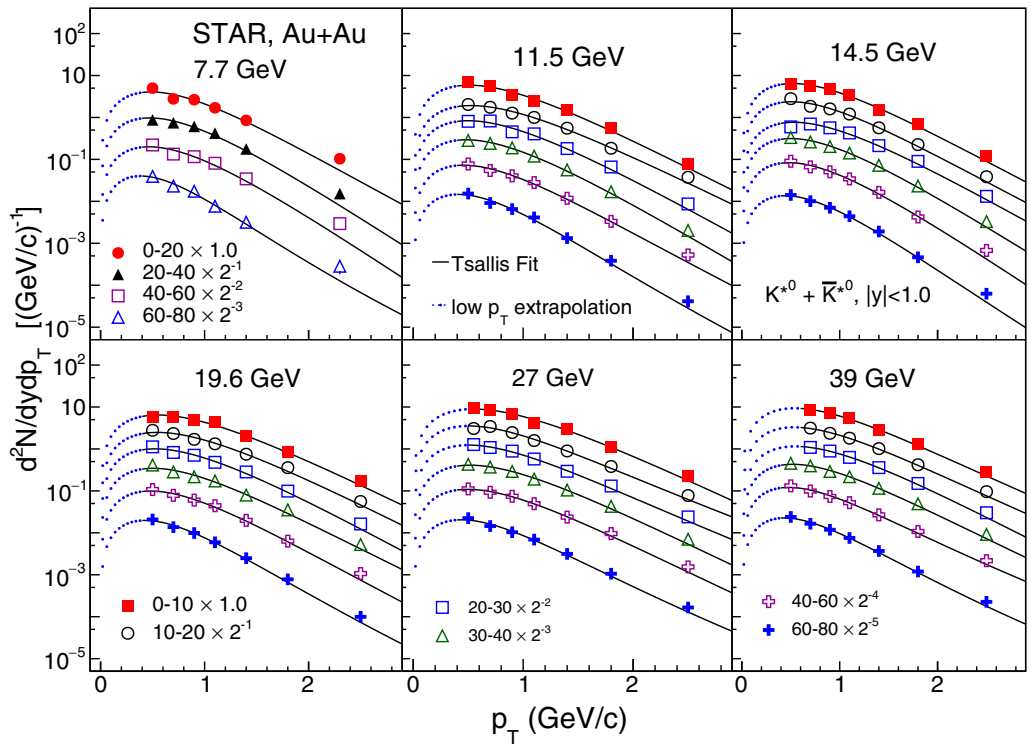

FIG. 3. K^{*0} transverse momentum (p_T) spectra at midrapidity ($|y| < 1$) for various collision centrality intervals in Au + Au collisions at $\sqrt{s_{NN}} = 7.7$, 11.5, 14.5, 19.6, 27, and 39 GeV. The solid and dashed lines indicate the Tsallis fit to the data and its extrapolation to the unmeasured low p_T region. The statistical and systematic uncertainties are within the marker size.

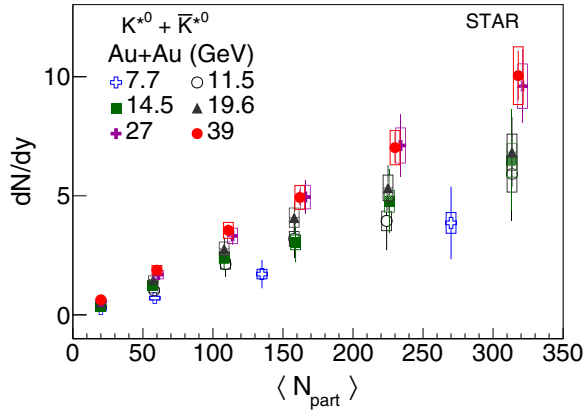

FIG. 4. Midrapidity yield of K^{*0} as a function of average number of participating nucleons in Au + Au collisions at $\sqrt{s_{NN}} = 7.7$, 11.5, 14.5, 19.6, 27, and 39 GeV. The vertical bars and open boxes respectively denote the statistical and systematic uncertainties.

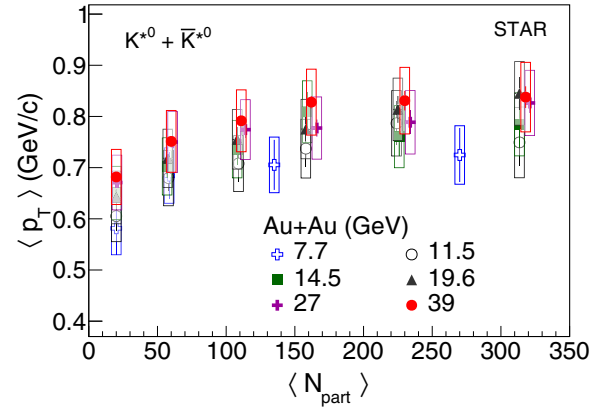

FIG. 6. The mean transverse momentum of K^{*0} as a function of $\langle N_{\rm part}\rangle$ in Au + Au collisions at $\sqrt{s_{NN}} = 7.7$, 11.5, 14.5, 19.6, 27, and 39 GeV. The vertical bars and open boxes respectively denote the statistical and systematic uncertainties.

compared with corresponding BES-I measurements of $K^{\pm}$, p, and $\bar{p}$ [34,37]. In contrast to $K^{\pm}$ and p, the normalized K^{*0} yield shows a weak dependence on centrality similar to $\bar{p}$.

In Fig. 6, the K^{*0} $\langle p_T\rangle$ is estimated using measured p_T spectra and extrapolated to the unmeasured p_T regions. The K^{*0} $\langle p_T\rangle$ is also compared with other identified particle species: π, K, and p as shown in Fig. 7. The $\langle p_T\rangle$ of K^{*0} is higher than pions and kaons and consistent with that of protons [34,37]. The trend suggests that the $\langle p_T\rangle$ is strongly coupled with the mass of the particle and consistent with previous RHIC observations [12–14]. Considering the systematic uncertainty that is not correlated in centrality bins (i.e., excluding the uncertainty in tracking efficiency ≈7.1% which is correlated among all centrality bins), the observed increase in $\langle p_T\rangle$ from peripheral to central collisions is consistent with expectations from increasing radial flow in more central collisions. Moreover, the contributions from hadronic rescattering can also increase $\langle p_T\rangle$ in central collisions [26]. Table III presents the dN/dy and $\langle p_T\rangle$ of $K^{*0} + \overline{K}^{*0}$ at different collision centrality intervals and beam energies.

C. Particle ratios

The ratios of resonances (K^{*0} and ϕ) to the nonresonances have been studied previously in small-system ($e + e$, $p + p$, $p + A$, and $d + A$) and heavy-ion ($A + A$) collisions. Such ratios are useful in understanding the late-stage interactions in heavy-ion collisions. Since the lifetime of K^{*0} and ϕ differ by about a factor of 10, their production can shed light on the different timescales of the evolution of the system in HIC.

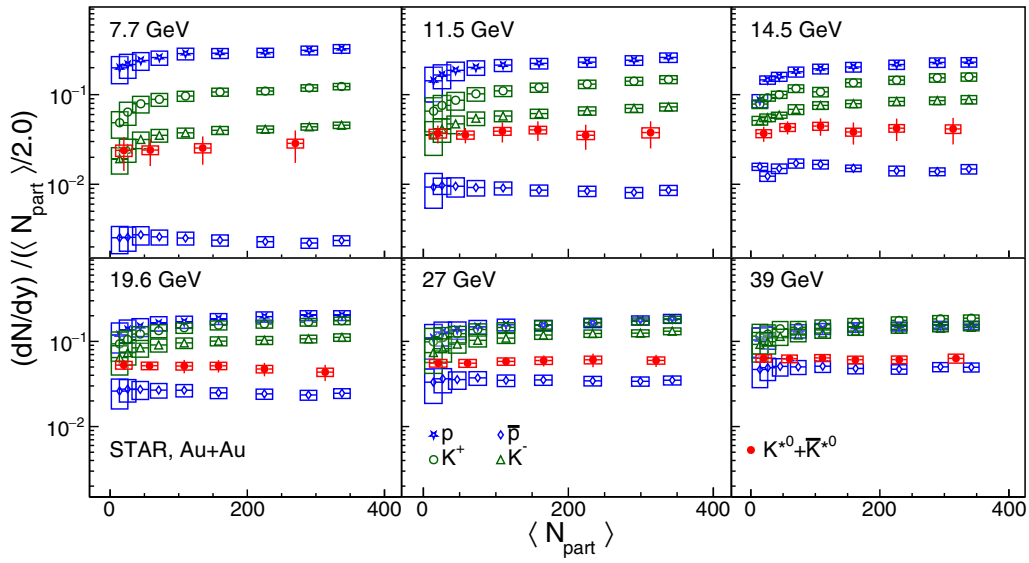

FIG. 5. Midrapidity yield per average number of participating nucleons for K^{*0}, $K^{\pm}$, p, and $\bar{p}$ as a function of $\langle N_{\rm part}\rangle$ from Au + Au collisions at $\sqrt{s_{NN}} = 7.7$, 11.5, 14.5, 19.6, 27, and 39 GeV. The vertical bars and open boxes denote the statistical and systematic uncertainties, respectively.

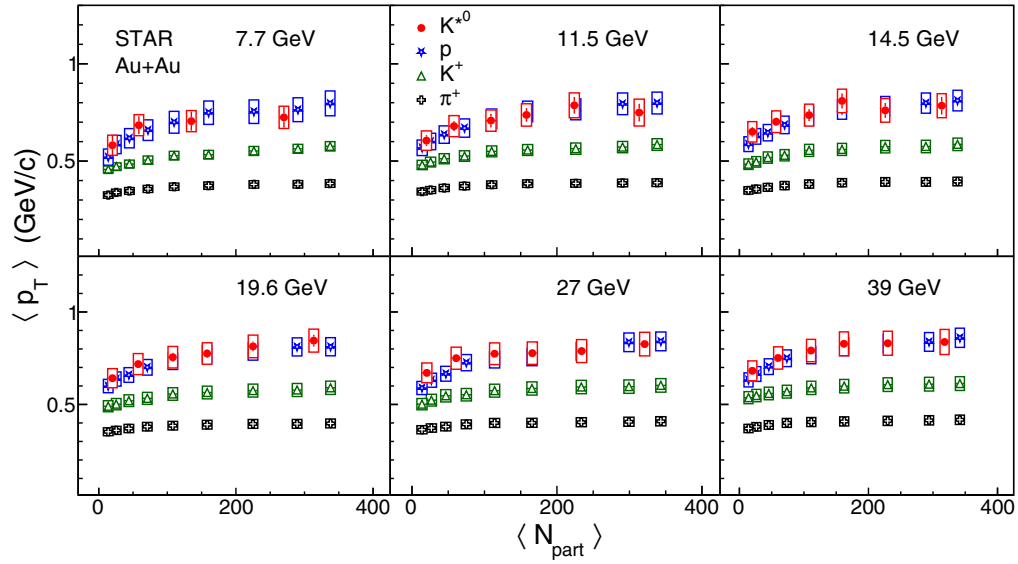

FIG. 7. The average transverse momentum of π, K, p [34,37], and K^{*0} as a function of average number of participating nucleons in Au + Au collisions at $\sqrt{s_{NN}} = 7.7$, 11.5, 14.5, 19.6, 27, and 39 GeV. The vertical bars and boxes denote the statistical and systematic uncertainties, respectively.

It is observed by the STAR, ALICE, and NA49 experiments that the K^{*0}/K ratio is smaller in central collisions than in peripheral (and small-system) collisions. While the ϕ/K ratio is observed to be independent of centrality, which is expected due to the longer lifetime of ϕ mesons. Figure 8 presents the K^{*0}/K $[= (K^{*0} + \overline{K}^{*0})/(K^+ + K^-)]$ ratio as a function of $\langle N_{\rm part}\rangle$ for six different beam energies. The charged kaon yields are taken from Refs. [34,37]. The BES-I results are compared with previously published STAR measurements in Au + Au collisions at $\sqrt{s_{NN}} = 62.4$ and 200 GeV [12,14]. The BES-I measurements follow the same centrality dependence as observed in previous measurements. From hanbury brown-twiss (HBT) studies, the variable $\langle dN_{\rm ch}/dy\rangle^{1/3}$ can be considered as a proxy for the system radius in heavy-ion collisions. If one assumes that the strength of rescattering is related to the distance traveled by the resonance decay products in the hadronic medium, then one naively expects K^{*0}/K ratio to decrease exponentially with $\langle dN_{\rm ch}/dy\rangle^{1/3}$ [18]. Figure 9 presents the K^{*0}/K ratio as a function of $\langle dN_{\rm ch}/dy\rangle^{1/3}$ for BES-I energies. These results are compared to previous measurements of different collision systems and beam energies from RHIC [12,14] and LHC [18–20,24]. Although present uncertainties in the data preclude any strong conclusion, we observe that the K^{*0}/K ratios from all BES energies follow the same behavior and those from LHC energies seem to be slightly larger. Figure 10 compares the K^{*0}/K and $\phi/K[= 2\phi/(K^+ + K^-)]$ [43] ratios in Au + Au collisions at $\sqrt{s_{NN}} =$ 7.7–39 GeV. Unlike K^{*0}/K, the ϕ/K ratio is mostly observed to be independent of collision centrality at these energies. The centrality dependent trend of K^{*0}/K and ϕ/K ratio is consistent with the expectation of more rescattering in more central collisions for K^{*0} daughters.

The measurement of K^{*0}/K ratio in a broad beam energy range may provide information on production mechanisms, especially the energy dependence of the relative strength of rescattering and regeneration processes. Figure 11 presents the beam energy dependence of K^{*0}/K ratio in small-systems ($e + e$ [44–47], $p + p$ [12,48–50], d + Au [13], and p + Pb [51,52]) and in central heavy-ion (C + C, Si + Si, Au + Au, and Pb + Pb [12,14,16,18–20]) collisions. The K^{*0}/K ratio is independent of beam energy in small-system collisions. The data, with combined statistical and systematic uncertainties, is fitted to a straight line and the resulting value is 0.34 ± 0.01. The K^{*0}/K from STAR BES-I energy is found to be consistent with that from Pb + Pb collisions at $\sqrt{s_{NN}} = 17.3$ GeV by NA49 [16]. Overall, there is a suppression of K^{*0}/K ratio in central heavy-ion collisions relative to the small-system collisions. The smaller K^{*0}/K ratio in heavy-ion collisions compared to small-system collisions is consistent with the expectation from the dominance of rescattering over regeneration in most-central heavy-ion collisions.

Due to the dominance of rescattering over regeneration, the reaction $K^{*0} \leftrightarrow K\pi$ may not be in balance. Experimentally, we cannot measure the particle yield ratios at different freeze-outs. Thus we make the approximation that the $(K^{*0}/K)_{\rm CFO}$ and $(K^{*0}/K)_{\rm KFO}$ are the same as the K^{*0}/K ratio measured in elementary and heavy-ion collisions, respectively. Furthermore, we assume that (i) all K^{*0} decayed before kinetic freeze-out are lost due to rescattering and (ii) no K^{*0} regeneration occurs between the chemical and kinetic freeze-out. Under these assumptions, the K^{*0}/K ratio at different freeze-outs are related in the following way [11]:

$$\left(\frac{K^{*0}}{K}\right)_{\rm KFO} = \left(\frac{K^{*0}}{K}\right)_{\rm CFO} \times e^{-\Delta t/\tau_{K^{*0}}}, \tag{6}$$

where $\tau_{K^{*0}}$ is the lifetime of K^{*0} (≈ 4.16 fm/c) and Δt is the lower limit of the time difference between CFO and KFO. It has been shown by AMPT calculations that such assumptions

TABLE III. dN/dy and $\langle p_T \rangle$ of $K^{*0} + \overline{K}^{*0}$, $(K^{*0} + \overline{K}^{*0})/(K^+ + K^-)$ ratio at $\sqrt{s_{NN}} = 7.7$–39 GeV. The uncertainties represent statistical and systematic uncertainties, respectively.

$\sqrt{s_{NN}}$ (GeV)	Centrality	dN/dy	$\langle p_T \rangle$ (GeV/c)	K^{*0}/K
	0–20%	$3.86 \pm 1.52 \pm 0.43$	$0.725 \pm 0.052 \pm 0.057$	$0.167 \pm 0.066 \pm 0.018$
	20–40%	$1.71 \pm 0.59 \pm 0.2$	$0.705 \pm 0.048 \pm 0.054$	$0.178 \pm 0.062 \pm 0.021$
7.7	40–60%	$0.70 \pm 0.23 \pm 0.07$	$0.684 \pm 0.045 \pm 0.054$	$0.203 \pm 0.068 \pm 0.027$
	60–80%	$0.24 \pm 0.10 \pm 0.04$	$0.581 \pm 0.051 \pm 0.051$	$0.297 \pm 0.122 \pm 0.060$
	0–10%	$5.92 \pm 1.98 \pm 0.76$	$0.750 \pm 0.045 \pm 0.069$	$0.173 \pm 0.058 \pm 0.022$
	10–20%	$3.94 \pm 1.22 \pm 0.41$	$0.786 \pm 0.042 \pm 0.063$	$0.177 \pm 0.055 \pm 0.018$
11.5	20–30%	$3.19 \pm 0.78 \pm 0.30$	$0.737 \pm 0.035 \pm 0.057$	$0.220 \pm 0.054 \pm 0.022$
	30–40%	$2.13 \pm 0.53 \pm 0.21$	$0.707 \pm 0.034 \pm 0.054$	$0.230 \pm 0.058 \pm 0.025$
	40–60%	$1.03 \pm 0.20 \pm 0.10$	$0.679 \pm 0.025 \pm 0.054$	$0.238 \pm 0.046 \pm 0.031$
	60–80%	$0.37 \pm 0.08 \pm 0.04$	$0.605 \pm 0.028 \pm 0.049$	$0.332 \pm 0.075 \pm 0.063$
	0–10%	$6.49 \pm 2.13 \pm 0.70$	$0.784 \pm 0.045 \pm 0.061$	$0.170 \pm 0.056 \pm 0.018$
	10–20%	$4.77 \pm 1.34 \pm 0.46$	$0.760 \pm 0.038 \pm 0.060$	$0.184 \pm 0.051 \pm 0.018$
14.5	20–30%	$3.04 \pm 0.84 \pm 0.30$	$0.809 \pm 0.038 \pm 0.060$	$0.178 \pm 0.049 \pm 0.018$
	30–40%	$2.40 \pm 0.53 \pm 0.24$	$0.736 \pm 0.030 \pm 0.056$	$0.220 \pm 0.048 \pm 0.022$
	40–60%	$1.23 \pm 0.20 \pm 0.12$	$0.702 \pm 0.022 \pm 0.055$	$0.246 \pm 0.040 \pm 0.024$
	60–80%	$0.36 \pm 0.07 \pm 0.03$	$0.650 \pm 0.025 \pm 0.052$	$0.261 \pm 0.050 \pm 0.026$
	0–10%	$6.83 \pm 1.47 \pm 0.75$	$0.845 \pm 0.031 \pm 0.062$	$0.154 \pm 0.033 \pm 0.017$
	10–20%	$5.33 \pm 0.95 \pm 0.53$	$0.813 \pm 0.026 \pm 0.061$	$0.180 \pm 0.032 \pm 0.018$
19.6	20–30%	$4.08 \pm 0.67 \pm 0.40$	$0.775 \pm 0.023 \pm 0.058$	$0.201 \pm 0.033 \pm 0.021$
	30–40%	$2.77 \pm 0.50 \pm 0.28$	$0.755 \pm 0.024 \pm 0.058$	$0.213 \pm 0.038 \pm 0.024$
	40–60%	$1.48 \pm 0.16 \pm 0.15$	$0.718 \pm 0.015 \pm 0.057$	$0.238 \pm 0.026 \pm 0.031$
	60–80%	$0.52 \pm 0.06 \pm 0.05$	$0.641 \pm 0.014 \pm 0.051$	$0.312 \pm 0.035 \pm 0.056$
	0–10%	$9.60 \pm 1.56 \pm 0.93$	$0.826 \pm 0.018 \pm 0.063$	$0.195 \pm 0.032 \pm 0.018$
	10–20%	$7.11 \pm 1.28 \pm 0.73$	$0.788 \pm 0.022 \pm 0.062$	$0.209 \pm 0.038 \pm 0.021$
27	20–30%	$4.95 \pm 0.72 \pm 0.49$	$0.777 \pm 0.016 \pm 0.060$	$0.216 \pm 0.031 \pm 0.022$
	30–40%	$3.31 \pm 0.36 \pm 0.32$	$0.774 \pm 0.015 \pm 0.058$	$0.228 \pm 0.025 \pm 0.024$
	40–60%	$1.69 \pm 0.14 \pm 0.18$	$0.750 \pm 0.011 \pm 0.060$	$0.240 \pm 0.020 \pm 0.031$
	60–80%	$0.57 \pm 0.04 \pm 0.06$	$0.670 \pm 0.010 \pm 0.053$	$0.300 \pm 0.023 \pm 0.058$
	0–10%	$10.04 \pm 1.04 \pm 1.21$	$0.837 \pm 0.021 \pm 0.067$	$0.191 \pm 0.020 \pm 0.022$
	10–20%	$7.02 \pm 0.65 \pm 0.71$	$0.830 \pm 0.019 \pm 0.065$	$0.194 \pm 0.018 \pm 0.020$
39	20–30%	$4.92 \pm 0.33 \pm 0.49$	$0.828 \pm 0.012 \pm 0.064$	$0.202 \pm 0.013 \pm 0.021$
	30–40%	$3.54 \pm 0.25 \pm 0.33$	$0.791 \pm 0.010 \pm 0.060$	$0.225 \pm 0.016 \pm 0.023$
	40–60%	$1.87 \pm 0.09 \pm 0.19$	$0.751 \pm 0.006 \pm 0.060$	$0.241 \pm 0.012 \pm 0.031$
	60–80%	$0.63 \pm 0.03 \pm 0.06$	$0.681 \pm 0.006 \pm 0.053$	$0.290 \pm 0.015 \pm 0.052$

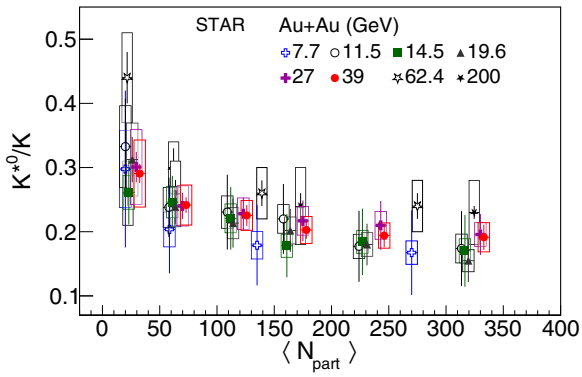

FIG. 8. K^{*0}/K ratio at midrapidity as a function of average number of participating nucleons in Au + Au collisions at $\sqrt{s_{NN}} =$ 7.7, 11.5, 14.5, 19.6, 27, and 39 GeV. The vertical bars and open boxes respectively denote the statistical and systematic uncertainties. The results are compared with previously published STAR [12,14] measurements.

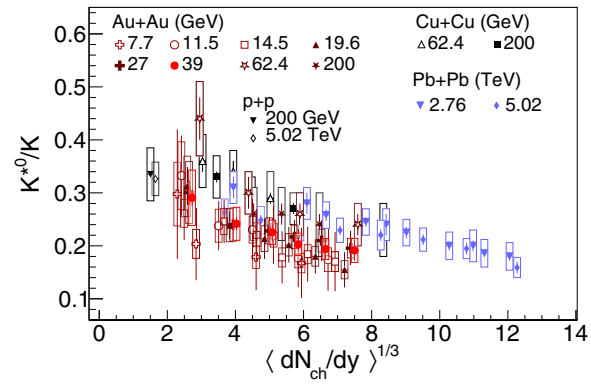

FIG. 9. K^{*0}/K ratio at midrapidity as a function of $\langle dN_{\rm ch}/dy \rangle^{1/3}$ in Au + Au collisions at $\sqrt{s_{NN}} = 7.7$, 11.5, 14.5, 19.6, 27, and 39 GeV. The vertical bars and open boxes respectively denote the statistical and systematic uncertainties. The results are compared with previously published STAR [12,14] and ALICE [18–20,24] measurements.

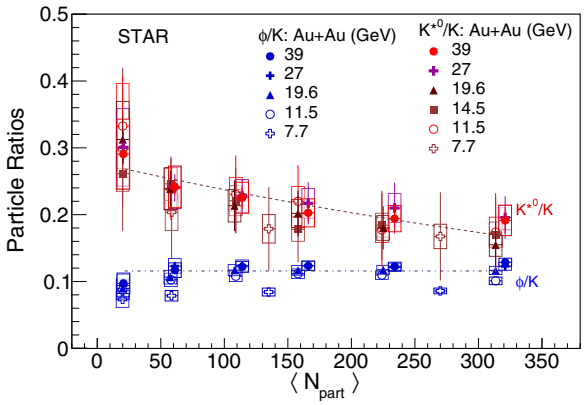

FIG. 10. Comparison of K^{*0}/K and ϕ/K [43] ratio at midrapidity as a function of average number of participating nucleons in Au + Au collisions at $\sqrt{s_{NN}}$ = 7.7–39 GeV. The vertical bars and boxes respectively denote the statistical and systematic uncertainties. The dashed lines are used to guide the eyes.

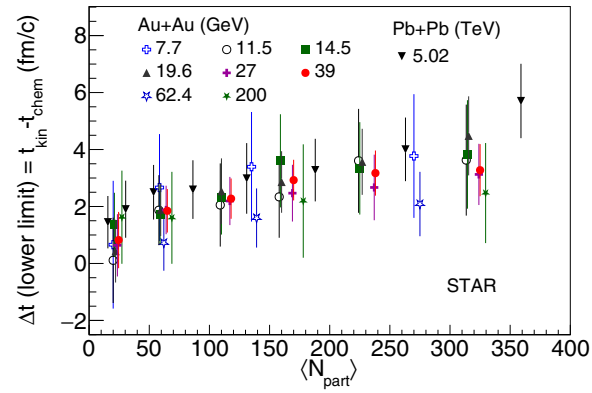

FIG. 12. The lower limit on the time difference (Δt) between the chemical and kinetic freeze-out as a function of average number of participating nucleons ($\langle N_{\rm part}\rangle$). The results are compared with previous STAR [12,14] and ALICE [18–20] measurements. The bars denote combined statistical and systematic uncertainties which is propagated from the uncertainties in K^{*0}/K ratio.

are applicable [27]. Due to the unavailability of small-system collisions at BES-I energies, the $(K^{*0}/K)_{\rm CFO}$ is taken from the straight-line fit through the global small-system data ($e+e$ and $p+p$ data shown in Fig. 11). The $(K^{*0}/K)_{\rm KFO}$ values are taken from the K^{*0}/K measurements at BES-I energies. The estimated Δt is boosted by the Lorentz factor [27]. Figure 12 presents the lower limit of the time difference between chemical and kinetic freeze-out as a function of $\langle N_{\rm part}\rangle$. The Δt from BES-I energies are compared with the results from Au + Au collisions at 62.4 and 200 GeV [12,14] and Pb + Pb collisions at 5.02 TeV [20]. The Δt from BES-I seems to follow the trend observed in previous RHIC and LHC data. Present uncertainty in BES-I data does not allow determination of the energy dependence of Δt. Future high-statistics BES-II measurements will offer better precision.

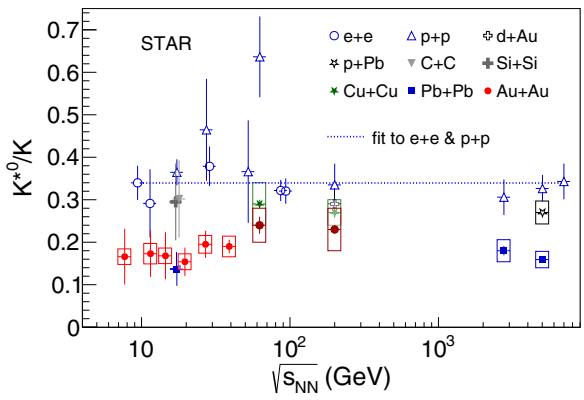

FIG. 11. The beam energy dependence of K^{*0}/K ratio in $e+e$ [44–47], $p+p$ [12,48–50], $d+$Au [13], $p+$Au [51,52], and most-central C + C, Si + Si [16], Au + Au [12,14], and Pb + Pb [18–20] collisions. For $e+e$ and $p+p$ collisions, the bars denote the quadratic sum of statistical and systematic uncertainties. For $p+A$ and $A+A$ data, the bars denote the statistical uncertainties and the boxes denote the systematic uncertainties.

IV. CONCLUSION

In summary, we presented the p_T spectra, dN/dy, and $\langle p_T\rangle$ of K^{*0} at midrapidity in Au + Au collisions at $\sqrt{s_{NN}}$ = 7.7–39 GeV using the first phase of RHIC beam energy scan data. For BES-I energies, the K^{*0} $\langle p_T\rangle$ is larger than that of pions and kaons and comparable to that of protons, indicating a mass dependence of $\langle p_T\rangle$. The K^{*0}/K ratio in the most-central Au + Au collisions is smaller than the same in small-system collision data. The K^{*0}/K ratio shows a weak centrality dependence and follows the same trend observed by previous RHIC and LHC measurements. On the contrary, the ϕ/K ratio is mostly independent of centrality. These observations support the scenario of the dominance of hadronic rescattering over regeneration for K^{*0} at BES energies. Based on the K^{*0}/K ratio, the lower limit of the time between chemical and kinetic freeze-out at BES energies is estimated. The high statistics data from the second phase of BES (BES-II) will allow more precise measurements of hadronic resonances at these energies.

ACKNOWLEDGMENTS

We thank the RHIC Operations Group and RCF at BNL, the NERSC Center at LBNL, and the Open Science Grid consortium for providing resources and support. This work was supported in part by the Office of Nuclear Physics within the U.S. DOE Office of Science, the U.S. National Science Foundation, National Natural Science Foundation of China, Chinese Academy of Science, the Ministry of Science and Technology of China and the Chinese Ministry of Education, the Higher Education Sprout Project by Ministry of Education at NCKU, the National Research Foundation of Korea, Czech Science Foundation and Ministry of Education, Youth and Sports of the Czech Republic, Hungarian National Research, Development and Innovation Office, New National Excellency Programme of the Hungarian Ministry of Human Capacities, Department of Atomic Energy and Department of Science and

Technology of the Government of India, the National Science Centre and WUT ID-UB of Poland, the Ministry of Science, Education and Sports of the Republic of Croatia, German Bundesministerium für Bildung, Wissenschaft, Forschung and Technologie (BMBF), Helmholtz Association, Ministry of Education, Culture, Sports, Science, and Technology (MEXT), and Japan Society for the Promotion of Science (JSPS).

[1] G. E. Brown and M. Rho, Scaling Effective Lagrangians in a Dense Medium, Phys. Rev. Lett. **66**, 2720 (1991).
[2] R. Rapp and E. V. Shuryak, Resolving the Anti-Baryon Production Puzzle in High-Energy Heavy Ion Collisions, Phys. Rev. Lett. **86**, 2980 (2001).
[3] C. Song and V. Koch, Chemical relaxation time of pions in hot hadronic matter, Phys. Rev. C **55**, 3026 (1997).
[4] J. Rafelski, J. Letessier, and G. Torrieri, Strange hadrons and their resonances: A Diagnostic tool of QGP freezeout dynamics, Phys. Rev. C **64**, 054907 (2001); **65**, 069902(E) (2002).
[5] F. Becattini, J. Manninen, and M. Gazdzicki, Energy and system size dependence of chemical freeze-out in relativistic nuclear collisions, Phys. Rev. C **73**, 044905 (2006).
[6] J. Cleymans, A. Forster, H. Oeschler, K. Redlich, and F. Uhlig, On the chemical equilibration of strangeness-exchange reaction in heavy-ion collisions, Phys. Lett. B **603**, 146 (2004).
[7] A. Andronic, P. Braun-Munzinger, and J. Stachel, Hadron production in central nucleus-nucleus collisions at chemical freeze-out, Nucl. Phys. A **772**, 167 (2006).
[8] S. D. Protopopescu, M. Alston-Garnjost, A. Barbaro-Galtieri, Stanley M. Flatte, J. H. Friedman, T. A. Lasinski, G. R. Lynch, M. S. Rabin, and F. T. Solmitz, Pi pi partial wave analysis from reactions pi + *p*—> pi+ pi- Delta + + and pi + *p*—> K+ K- Delta + + at 7.1-GeV/*c*, Phys. Rev. D **7**, 1279 (1973).
[9] M. J. Matison, A. Barbaro-Galtieri, M. Alston-Garnjost, S. M. Flatte, J. H. Friedman, G. R. Lynch, M. S. Rabin, and F. T. Solmitz, Study of *K*+ pi- scattering in the reaction *K* + *p*— > *K*+ pi- Delta + + at 12-GeV/*c*, Phys. Rev. D **9**, 1872 (1974).
[10] M. Bleicher *et al.*, Relativistic hadron hadron collisions in the ultrarelativistic quantum molecular dynamics model, J. Phys. G **25**, 1859 (1999).
[11] C. Adler *et al.*, *K**(892)0 production in relativistic heavy ion collisions at $\sqrt{s_{NN}} = 130$ GeV, Phys. Rev. C **66**, 061901 (2002).
[12] J. Adams *et al.*, *K*(892)* resonance production in Au+Au and $p + p$ collisions at $\sqrt{s_{NN}} = 200$ GeV at STAR, Phys. Rev. C **71**, 064902 (2005).
[13] B. I. Abelev *et al.*, Hadronic resonance production in $d +$ Au collisions at $\sqrt{s_{NN}} = 200$ GeV at RHIC, Phys. Rev. C **78**, 044906 (2008).
[14] M. M. Aggarwal *et al.*, K^{*0} production in Cu+Cu and Au+Au collisions at $\sqrt{s_{NN}} = 62.4$ GeV and 200 GeV, Phys. Rev. C **84**, 034909 (2011).
[15] A. Adare *et al.*, Measurement of K^0_S and K^{*0} in $p + p$, $d +$ Au, and Cu+Cu collisions at $\sqrt{s_{NN}} = 200$ GeV, Phys. Rev. C **90**, 054905 (2014).
[16] T. Anticic *et al.*, $K^*(892)^0$ and $\bar{K}^*(892)^0$ production in central Pb+Pb, Si+Si, C+C, and inelastic $p + p$ collisions at 158*A* GeV, Phys. Rev. C **84**, 064909 (2011).
[17] A. Aduszkiewicz *et al.*, $K^*(892)^0$ meson production in inelastic p+p interactions at 158 GeV/c beam momentum measured by NA61/SHINE at the CERN SPS, Eur. Phys. J. C **80**, 460 (2020).
[18] B. B. Abelev *et al.*, $K^*(892)^0$ and $\phi(1020)$ production in Pb-Pb collisions at $\sqrt{s_{NN}} = 2.76$ TeV, Phys. Rev. C **91**, 024609 (2015).
[19] J. Adam *et al.*, $K^*(892)^0$ and $\phi(1020)$ meson production at high transverse momentum in pp and Pb-Pb collisions at $\sqrt{s_{NN}} =$ 2.76 TeV, Phys. Rev. C **95**, 064606 (2017).
[20] S. Acharya *et al.*, Evidence of rescattering effect in Pb-Pb collisions at the LHC through production of $K^*(892)^0$ and $\phi(1020)$ mesons, Phys. Lett. B **802**, 135225 (2020).
[21] B. Abelev *et al.*, Production of $K^*(892)^0$ and $\phi(1020)$ in pp collisions at $\sqrt{s} = 7$ TeV, Eur. Phys. J. C **72**, 2183 (2012).
[22] S. Acharya *et al.*, $K^*(892)^0$ and $\phi(1020)$ production at midrapidity in pp collisions at $\sqrt{s} = 8$ TeV, Phys. Rev. C **102**, 024912 (2020).
[23] S. Acharya *et al.*, Multiplicity dependence of K $*$ $(892)^0$ and $\phi(1020)$ production in pp collisions at $\sqrt{s} = 13$ TeV, Phys. Lett. B **807**, 135501 (2020).
[24] S. Acharya *et al.*, Production of $K^*(892)^0$ and $\phi(1020)$ in pp and Pb-Pb collisions at $\sqrt{s_{NN}} = 5.02$ TeV, Phys. Rev. C **106**, 034907 (2022).
[25] M. Bleicher and J. Aichelin, Strange resonance production: Probing chemical and thermal freezeout in relativistic heavy ion collisions, Phys. Lett. B **530**, 81 (2002).
[26] A. G. Knospe, C. Markert, K. Werner, J. Steinheimer, and M. Bleicher, Hadronic resonance production and interaction in partonic and hadronic matter in the EPOS3 model with and without the hadronic afterburner UrQMD, Phys. Rev. C **93**, 014911 (2016).
[27] S. Singha, B. Mohanty, and Z.-W. Lin, Studying re-scattering effect in heavy-ion collision through K* production, Int. J. Mod. Phys. E **24**, 1550041 (2015).
[28] K. H. Ackermann *et al.*, STAR detector overview, Nucl. Instrum. Methods A **499**, 624 (2003).
[29] G. Contin *et al.*, The STAR MAPS-based PiXeL detector, Nucl. Instrum. Methods A **907**, 60 (2018).
[30] M. Anderson *et al.*, The Star time projection chamber: A Unique tool for studying high multiplicity events at RHIC, Nucl. Instrum. Methods A **499**, 659 (2003).
[31] W. J. Llope *et al.*, The TOFp / pVPD time-of-flight system for STAR, Nucl. Instrum. Methods A **522**, 252 (2004).
[32] B. Bonner, H. Chen, G. Eppley, F. Geurts, J. Lamas Valverde, C. Li, W. J. Llope, T. Nussbaum, E. Platner, and J. Roberts, A single Time-of-Flight tray based on multigap resistive plate chambers for the STAR experiment at RHIC, Nucl. Instrum. Methods A **508**, 181 (2003).
[33] F. S. Bieser *et al.*, The STAR trigger, Nucl. Instrum. Methods A **499**, 766 (2003).
[34] J. Adam *et al.*, Bulk properties of the system formed in Au+Au collisions at $\sqrt{s_{NN}} = 14.5$ GeV at the BNL STAR detector, Phys. Rev. C **101**, 024905 (2020).
[35] L. Adamczyk *et al.*, Elliptic flow of identified hadrons in Au+Au collisions at $\sqrt{s_{NN}} = 7.7$–62.4 GeV, Phys. Rev. C **88**, 014902 (2013).

[36] M. L. Miller, K. Reygers, S. J. Sanders, and P. Steinberg, Glauber modeling in high energy nuclear collisions, Ann. Rev. Nucl. Part. Sci. **57**, 205 (2007).
[37] L. Adamczyk *et al.*, Bulk properties of the medium produced in relativistic heavy-ion collisions from the beam energy scan program, Phys. Rev. C **96**, 044904 (2017).
[38] H. Bichsel, A method to improve tracking and particle identification in TPCs and silicon detectors, Nucl. Instrum. Methods A **562**, 154 (2006).
[39] M. Shao, O. Y. Barannikova, X. Dong, Y. Fisyak, L. Ruan, P. Sorensen, and Z. Xu, Extensive particle identification with TPC and TOF at the STAR experiment, Nucl. Instrum. Methods A **558**, 419 (2006).
[40] P. A. Zyla *et al.*, Review of particle physics, Progr. Theor. Exp. Phys. **2020**, 083C01 (2020).
[41] V. Fine and P. Nevski, Proc. CHEP 2000, 143 (2000).
[42] C. Tsallis, Possible generalization of Boltzmann-Gibbs statistics, J. Statist. Phys. **52**, 479 (1988).
[43] J. Adam *et al.*, Strange hadron production in Au+Au collisions at $\sqrt{s_{NN}} = 7.7$, 11.5, 19.6, 27, and 39 GeV, Phys. Rev. C **102**, 034909 (2020).
[44] H. Albrecht *et al.*, Inclusive production of $K^*(892)$, $\rho^0(770)$, and $\omega(783)$ mesons in the Υ energy region, Z. Phys. C **61**, 1 (1994).
[45] Y.-J. Pei, A Simple approach to describe hadron production rates in $e + e$- annihilation, Z. Phys. C **72**, 39 (1996).
[46] W. Hofmann, Particle composition in hadronic jets in e^+e^- annihilation, Ann. Rev. Nucl. Part. Sci. **38**, 279 (1988).
[47] K. Abe *et al.*, Production of pi+, $K+$, $K0$, $K*0$, phi, p and Lambda0 in hadronic Z0 decays, Phys. Rev. D **59**, 052001 (1999).
[48] M. Aguilar-Benitez *et al.*, Inclusive particle production in 400-GeV/c p p interactions, Z. Phys. C **50**, 405 (1991).
[49] D. Drijard *et al.*, Production of vector and tensor mesons in proton proton collisions at $\sqrt{s} = 52.5$-GeV, Z. Phys. C **9**, 293 (1981).
[50] T. Akesson *et al.*, Inclusive vector-meson production in the central region of pp collisions at $\sqrt{s} = 63$-GeV, Nucl. Phys. B **203**, 27 (1982); **229**, 541(E) (1983).
[51] J. Adam *et al.*, Production of $K^*(892)^0$ and $\phi(1020)$ in p–Pb collisions at $\sqrt{s_{NN}} = 5.02$ TeV, Eur. Phys. J. C **76**, 245 (2016).
[52] S. Acharya *et al.*, $K^*(892)^0$ and $\phi(1020)$production in p-Pb collisions at $\sqrt{s_{NN}} = 8.16$ TeV, arXiv:2110.10042.